UNIVERSITY OF AMSTERDAM

UvA-DARE (Digital Academic Repository)

Protein aggregates act as a deterministic disruptor during bacterial cell size homeostasis

Mortier, J.; Govers, S.K.; Cambré, A.; Van Eyken, R.; Verheul, J.; den Blaauwen, T.; Aertsen, A.

DOI
10.1007/s00018-023-05002-4

Publication date
2023

Document Version
Final published version

Published in
Cellular and Molecular Life Sciences

License
Article 25fa Dutch Copyright Act (https://www.openaccess.nl/en/in-the-netherlands/you-share-we-take-care)

Link to publication

Citation for published version (APA):
Mortier, J., Govers, S. K., Cambré, A., Van Eyken, R., Verheul, J., den Blaauwen, T., & Aertsen, A. (2023). Protein aggregates act as a deterministic disruptor during bacterial cell size homeostasis. *Cellular and Molecular Life Sciences*, *80*(12), Article 360. https://doi.org/10.1007/s00018-023-05002-4

General rights
It is not permitted to download or to forward/distribute the text or part of it without the consent of the author(s) and/or copyright holder(s), other than for strictly personal, individual use, unless the work is under an open content license (like Creative Commons).

Disclaimer/Complaints regulations
If you believe that digital publication of certain material infringes any of your rights or (privacy) interests, please let the Library know, stating your reasons. In case of a legitimate complaint, the Library will make the material inaccessible and/or remove it from the website. Please Ask the Library: https://uba.uva.nl/en/contact, or a letter to: Library of the University of Amsterdam, Secretariat, Singel 425, 1012 WP Amsterdam, The Netherlands. You will be contacted as soon as possible.

UvA-DARE is a service provided by the library of the University of Amsterdam (https://dare.uva.nl)

Download date:27 May 2024

Cellular and Molecular Life Sciences (2023) 80:360
https://doi.org/10.1007/s00018-023-05002-4

ORIGINAL ARTICLE

Protein aggregates act as a deterministic disruptor during bacterial cell size homeostasis

Julien Mortier[1] · Sander K. Govers[1,2] · Alexander Cambré[1] · Ronald Van Eyken[1] · Jolanda Verheul[3] · Tanneke den Blaauwen[3] · Abram Aertsen[1]

Received: 2 May 2023 / Revised: 13 October 2023 / Accepted: 15 October 2023 / Published online: 16 November 2023
© The Author(s), under exclusive licence to Springer Nature Switzerland AG 2023

Abstract

Mechanisms underlying deviant cell size fluctuations among clonal bacterial siblings are generally considered to be cryptic and stochastic in nature. However, by scrutinizing heat-stressed populations of the model bacterium *Escherichia coli*, we uncovered the existence of a deterministic asymmetry in cell division that is caused by the presence of intracellular protein aggregates (PAs). While these structures typically locate at the cell pole and segregate asymmetrically among daughter cells, we now show that the presence of a polar PA consistently causes a more distal off-center positioning of the FtsZ division septum. The resulting increased length of PA-inheriting siblings persists over multiple generations and could be observed in both *E. coli* and *Bacillus subtilis* populations. Closer investigation suggests that a PA can physically perturb the nucleoid structure, which subsequently leads to asymmetric septation.

Keywords *Escherichia coli* · *Bacillus subtilis* · Binary fission · Protein aggregates · Asymmetric septation

Introduction

While cell sizes among different bacterial species can span several orders of magnitude [1], they are maintained within a very narrow distribution among the siblings of a clonal bacterial population through the coordinated interplay between cell growth and division. Indeed, possible cell size deviations seem to be intrinsically corrected over one or several generations when binary fission is systematically triggered after growing to a specific cell size (i.e., "sizer" model) or after the addition of a fixed cell volume (i.e., "adder" model) [2–7]. Furthermore, the exact midcell positioning of an FtsZ proto-ring (where it recruits proteins involved in cell wall synthesis and cell septation) [8] minimizes cell size fluctuations at birth and is coordinated by the oscillating Min system [9], SlmA-based nucleoid occlusion [10–13] and *ter*-mediated linkage of the dividing chromosome to the FtsZ proto-ring [14–18]. These homeostatic mechanisms ensure that cell sizes are fine-tuned in changing environmental conditions and that individual cell sizes do not continuously diverge with every generation of a growing lineage [2, 4, 19–21].

While several environmental conditions such as DNA-damage [22], nutrient availability [23–27], and osmotic forces [28] have been shown to influence cell size on the population level, understanding the origins of intercellular size variations within a homogeneous environment (i.e., not arising from local spatio-temporal gradients) has remained elusive. For example, the so-called "growth law" states that there is a positive correlation between the population-average cell size and the population-average growth rate across a variety of growth conditions [23, 24], but this relationship does not seem to reliably persist on the single-cell level (i.e., single-cell variability in growth rate does not correlate well with single-cell variability in cell size within a particular population) [6]. Single-cell fluctuations in cell size are, therefore, generally assumed to be purely stochastic in nature and to stem from stochastic occurrences of asymmetric divisions and variability in the speed and timing of cell constriction [29].

✉ Abram Aertsen
abram.aertsen@kuleuven.be

[1] Department of Microbial and Molecular Systems, KU Leuven, Leuven, Belgium

[2] Department of Biology, KU Leuven, Leuven, Belgium

[3] Swammerdam Institute for Life Sciences, Bacterial Cell Biology and Physiology, University of Amsterdam, Amsterdam, The Netherlands

In this study, however, we discovered that intracellular protein aggregates (PAs) can act as a deterministic disruptor of the cell size homeostasis process in *Escherichia coli* and *Bacillus subtilis* model systems. These PA structures emerge from the assembly of misfolded proteins caused by adverse environmental stresses, translational errors or mutations [30]. Moreover, they are typically associated with the old cell pole (i.e., the cell pole that was inherited from the mother cell and was not newly formed during division) due to an inability to migrate past the nucleoid and the resulting asymmetric segregation that occurs during cell division [30–35]. We observed that these PAs impact the intracellular architecture by disrupting the location and characteristics of the nucleoid and division machinery, thereby perturbing the cell's ability to accurately determine its mid-point and leading to a structural increase in cell size for daughter cells inheriting these structures.

Results

PAs cause systematic deviations from cell division symmetry

When comparing morphological characteristics of PA-bearing and PA-free *E. coli* MG1655 *ibpA-msfGFP* siblings (harboring the previously described fluorescent IbpA-msfGFP PA-reporter in which the small heat shock protein IbpA colocalizes with aggregated proteins [36]) 1 h after exposure to a PA-inducing sublethal heat shock, we noted that the PA-bearing subpopulation was on average 11.4% longer than the PA-free subpopulation (Fig. 1A). To address this observation more systematically, we monitored the divisions of PA-bearing cells in 30 MG1655 *ibpA-msfGFP* microcolonies emerging from heat-shocked founder cells with time-lapse fluorescence microscopy and determined the relative division site localization with respect to the old cell pole (Fig. 1B and C). Since PAs are preferentially found in the old cell poles, we used the divisions of the corresponding PA-free cells with the exact same old pole ages as a control. This analysis revealed that during division events where a PA is present in the old cell pole, the septation site tends to be asymmetrically skewed away from this PA-bearing cell pole

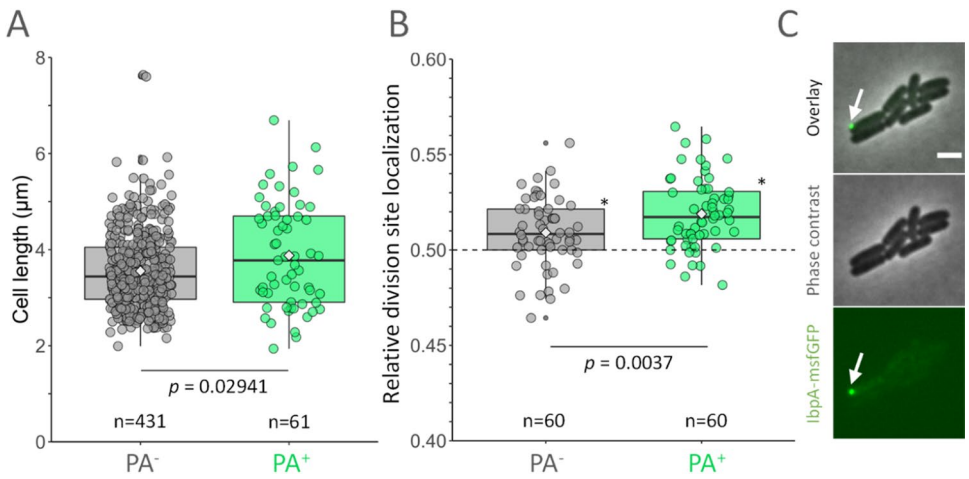

Fig. 1 **A** Cell lengths of PA-bearing (PA^+) and PA-free (PA^-) subpopulations of exponential phase *E. coli* MG1655 *ibpA-msfGFP* cells 1 h after exposure to a PA-inducing sublethal heat shock (47 °C, 15 min). These cells were transferred from well-mixed liquid cultures onto agarose pads for immediate microscopic image acquisition. The *p* value was calculated using a Welch's *t*-test comparing the PA^+ and PA^- subpopulations. **B** Normalized division site localization determined for division events where PA-bearing cells (PA^+) and the corresponding PA-free cells with the exact same old pole age (PA^-) in 3 generations of 30 MG1655 *ibpA-msfGFP* microcolonies asymmetrically segregating polarly localized heat shock induced PAs (47 °C, 15 min). The horizontal dashed line at 0.5 represents a perfectly symmetrical division, while values higher than 0.5 correspond to larger old pole cells at birth and values lower than 0.5 correspond to larger new pole cells at birth. The *p* value comparing the asymmetry of PA^+ and PA^- cell couples at birth was calculated using a Student's t test. Asterisks indicate a significant difference ($p \leq 0.05$) of each bin from 0.5 (Student's *t*-tests). **C** Representative phase contrast, epifluorescence (reporting the asymmetrically segregated IbpA-msfGFP labeled PA indicated by the white arrow) and superimposed images of *E. coli* MG1655 *ibpA-msfGFP* microcolonies 3 generations after a sublethal heat shock. Scale bar corresponds to 2 µm. For **A** and **B**, data were pooled from three independent experiments and is shown as box (25th to 75th percentile) and whisker (1.5×IQR) plots with individual data points overlaid as jitter plots, the mean plotted as a white diamond and the sample sizes (*n*) indicated on the figures

(Fig. 1B). Because of this asymmetry, PA-bearing siblings were systematically larger at birth than their PA-free sisters.

Surprisingly, a small inherent asymmetry was also observed in the corresponding PA-free division events, which manifested itself in a slight shift away from the (empty) old cell pole (Fig. 1B). Notably, besides the above-mentioned deterministic PA/old cell pole-associated effects, our analysis also again underscores the inherent stochasticity/inaccuracy in the cell's ability to place the division site at the exact mid-point of the cell, clearly visible by the variability within the PA-free divisional cells (Fig. 1B).

We subsequently hypothesized that the division asymmetry we observed in cells with heat shock-derived PAs would also occur in the recently described *E. coli* MG1655 *ibpA-msfGFP tnaA*$^{\Delta 106}$ strain, in which expression of the aggregation-prone TnaA$^{\Delta 106}$ variant (and as such the induction of IbpA-msfGFP labeled TnaA$^{\Delta 106}$ PAs) can be tightly controlled by L-tryptophan without the need of a heatshock [37]. All division events from 3 generations of microcolonies emerging from L-tryptophan-induced founder cells were monitored and categorized in 7 different division types (designated "1" through "7") according to the pattern of old/new cell pole inheritance (Fig. 2A and B). In short, if a mother cell's designation equals ×, its daughter cells receive a designation equal to 2× (if it inherits the old cell pole) or 2× + 1 (if it inherits the new cell pole) (Fig. 2A). This allows us to distinguish divisions based on the dividing cell's relationship to the asymmetrically segregating (and old cell pole-associated) PA, the age of the old cell pole (i.e., the number of generations it has been inherited) and the generation in which it occurs. This analysis clearly revealed that consecutive divisions of PA-inheriting cells systematically show strong deviations from symmetry (divisions "1", "2" and "4"; Fig. 2C and E) and seem to initiate division at a larger cell length (Fig. 2G). While small old pole-associated asymmetries were again detected in PA-free cells (found to be significant in divisions "3" and "6"; Fig. 2C and E), these were significantly less pronounced than those observed in PA-bearing cells. As a PA-free control, the analysis was repeated for the nearly isogenic *E. coli* MG1655 *ibpA-msfGFP tnaA*^{K270A} cells, which produce a soluble (i.e., non PA-forming) catalytically compromised TnaA variant [37, 38], confirming a small old pole-associated asymmetry in division, skewed away from the old cell pole (Fig. 2D and F). Note that the average cell length (i.e., independent of PA state or pole age) diminishes throughout the generations in these experiments (Fig. 2C and D), presumably due to changes in nutrient availability in the agarose pads.

These observations were also independently confirmed in *E. coli* MG1655 Δ*lacY* pTrc99A-P_{trc}-*mCer-cI78*^{EP8} and *E. coli* MG1655 Δ*lacY* pTrc99A-P_{trc}-*mCer-cI78*^{WT} microcolonies (Supplementary Fig. S1), in which fluorescently tagged synthetic proteins (aggregate-prone mCer-cI78^{EP8} or its soluble mCer-cI78^{WT} equivalent [36]) are expressed from IPTG-inducible plasmids. In turn, this suggests that the precise composition or origin of the PA is inconsequential to disrupting binary fission, but that the physical presence of these structures themselves constitutes the driving factor.

We subsequently hypothesized that this phenomenon of PA-mediated disruption of division symmetry may not be limited to *E. coli* but could extend to other rod-shaped bacteria that have a similar pattern of asymmetric PA inheritance. To test this, we used a recently described *B. subtilis* PA model system (manuscript under review) in which expression of aggregate-prone GFP(Sp)-cI78^{EP8} and soluble GFP(Sp)-cI78^{WT} are controlled by an IPTG-inducible promoter from the *amyE* locus (Supplementary Fig. S2A). This system allowed a similar analysis as in *E. coli* and confirmed the existence of a strong PA-mediated asymmetry during cell division (Supplementary Fig. S2B and D) and a small old pole-associated asymmetry in divisions where no PAs were observed (Supplementary Fig. S2C and E). In line with the previously mentioned *E. coli* experiments (Fig. 2G, Supplementary Fig. S1E), PA-bearing *B. subtilis* cells also divide at larger cell lengths than their PA-free counterparts (Supplementary Fig. S2F). Notably, we also observed that the asymmetric segregation of GFP(Sp)-cI78^{EP8} PAs seems to be accompanied by a PA-derived concentration gradient in the cells spawning off from the PA-harboring cell (Supplementary Fig. S2A), a phenomenon that has previously been described for *E. coli* and that may stem from a combination of disaggregation and segregation dynamics during growth and could shape the proteomes of individual cells in a deterministic lineage-dependent fashion [35, 36].

PAs displace the nucleoid and division machinery

We subsequently examined whether this PA-mediated disruption of cell division symmetry was actually caused by PA-driven repositioning of the cell division machinery and the localization of the nucleoid. Indeed, in L-tryptophan-induced *E. coli* MG1655 *ibpA-msfGFP tnaA*$^{\Delta 106}$ cells binned according to their cell cycle age (and oriented according to their most fluorescent pole), FtsZ was found to assemble in an asymmetrically located Z-ring in predivisional and divisional cells containing a single aggregate (Fig. 3A, B (left panels) and C; Supplementary Fig. S3A). In PA-free *E. coli* MG1655 *ibpA-msfGFP tnaA*^{K270A} control cells undergoing the same treatment, division symmetry was of course expected since these cell orientations can be assumed to be randomized when orienting cells according to their most fluorescent pole [Fig. 3A, B (left panels) and C; Supplementary Fig. S3A]. In addition, nucleoid positioning was found to be skewed away from the PA-containing cell pole throughout the cell cycle, resulting in a shift in the nucleoid-free interchromosomal space in predivisional and divisional cells

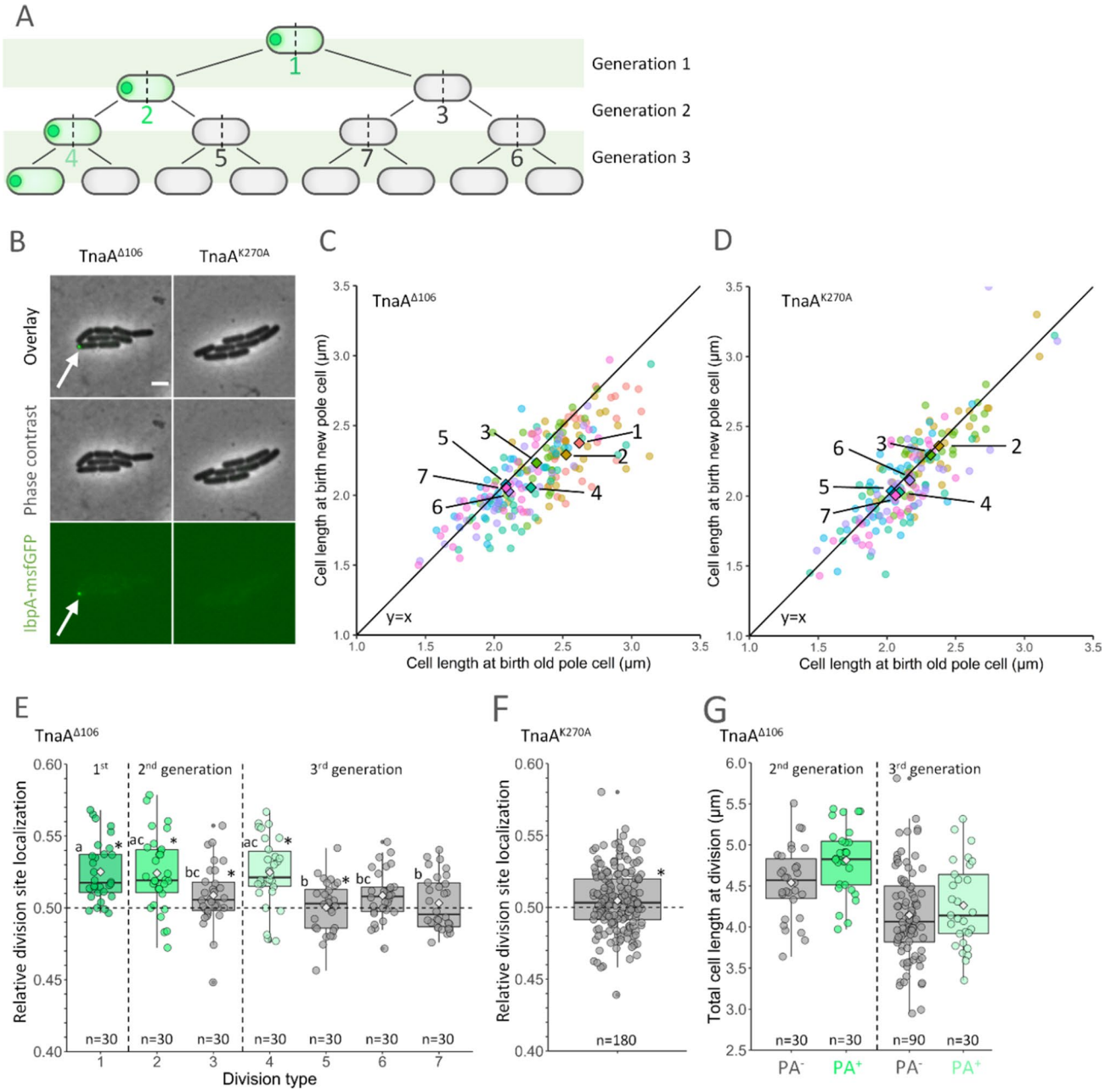

[Fig. 3A, B (left panels) and D; Supplementary Fig. S3A]. Strikingly, in cells harboring a PA in both cell poles, both the Z-ring and nucleoid placement were still found to be asymmetrically placed, yet skewed away from the largest (based on fluorescent intensity) aggregate [Fig. 3B (right panels), C and D; Supplementary Fig. S3]. This seems to indicate the presence of a size-dependent PA-mediated effect. In line with these findings in *E. coli*, we also found this shift in nucleoid positioning throughout the cell cycle for IPTG-induced *B. subtilis* PS832 *amyE*::$P_{Hyperspank}$ *gfp(Sp)-cI78*^{EP8} cells carrying a single PA, while symmetry was (as expected) observed in PA-free *B. subtilis* PS832 *amyE*::$P_{Hyperspank}$ *gfp(Sp)-cI78*^{WT} control cells (Supplementary Fig. S4A, B and C). Taken together, these observations suggest that aggregates compete for space with the nucleoid resulting in its effective displacement and a shift in the nucleoid-free space where FtsZ polymerization (i.e., Z-ring formation) is allowed by the nucleoid occlusion system.

It should be noted, however, that the averaged DAPI and FtsZ signal profiles of the fixed cells were oriented according to the IbpA-msfGFP signal in the cell (i.e., so that the poles containing the most IbpA-msfGFP or GFP(Sp)-cI78^{EP8} fluorescence become oriented to the left on Figs. 3, S3 and S4). As such, these poles may become enriched in old cell poles in PA-bearing cells, while this would not be the case for PA-free cells (where cell orientation would presumably

◂**Fig. 2** **A** Division types 1–7 were assigned according to their relation to the asymmetrically segregating PA, their inheritance of old or new cell poles and their generation as schematically shown here. **B** Representative phase contrast, epifluorescence (reporting IbpA-msfGFP localization) and superimposed images of *E. coli* MG1655 *ibpA-msfGFP tnaA*$^{\Delta 106}$ (left) and *E. coli* MG1655 *ibpA-msfGFP tnaA*^{K270A} (right) microcolonies 3 generations after induction with 1.25 mM L-tryptophan is halted. The asymmetrically segregated TnaA$^{\Delta 106}$ PA is indicated by a white arrow. Scale bar corresponds to 2 µm. **C**, **D** Scatterplot of the cell length at birth of old vs. new pole cells of all division events in 3 generations of 30 *E. coli* MG1655 *ibpA-msfGFP tnaA*$^{\Delta 106}$ (**C**; asymmetrically segregating old pole localized TnaA$^{\Delta 106}$ PAs in divisions 1, 2 and 4) and 30 *E. coli* MG1655 *ibpA-msfGFP tnaA*^{K270A} (**D**; no PAs; division type 1 omitted because old/new pole cells cannot be assigned) microcolonies. Each data point corresponds to a single-cell couple of sister cells at birth. Data points are binned according to their division type (see **A**; 1 red, 2 orange, 3 green, 4 teal, 5 blue, 6 purple, 7 pink) and the mean is plotted as a diamond in the corresponding color. The black line corresponds to the identity function ($y=x$) and represents a perfectly symmetrical division event. **E** Normalized division site localization determined for all division events in 3 generations of 30 *E. coli* MG1655 *ibpA-msfGFP tnaA*$^{\Delta 106}$ microcolonies asymmetrically segregating polarly localized TnaA$^{\Delta 106}$ PAs and binned according to their division type (see **A**). Lowercase letters indicate that pairwise comparisons between groups are statistically significant when the groups do not have any letter in common (ANOVA followed by Tukey HSD post-hoc test, p value ≤ 0.05). **F** Normalized division site localization determined for all division events in 3 generations of 30 *E. coli* MG1655 *ibpA-msfGFP tnaA*^{K270A} microcolonies (the first division event was excluded because the old and new cell poles could not be assigned). **G** Total cell length at birth at division PA-bearing (PA$^+$) and PA-free (PA$^-$) cells for generations 2 and 3 (see **A**) of 30 *E. coli* MG1655 *ibpA-msfGFP tnaA*$^{\Delta 106}$ microcolonies. Using ANOVA, a p-value ≤ 0.05 was obtained to show that the total cell length at birth of PA$^+$ cells is larger than for PA$^-$ cells. For **E** and **F**, the horizontal dashed line at 0.5 represents a perfectly symmetrical division, while values higher than 0.5 correspond to larger old pole cells at birth and values lower than 0.5 correspond to larger new pole cells at birth; asterisks indicate a significant difference ($p \leq 0.05$) of each bin from 0.5 (Student's t tests). For **C**–**G**, data was pooled from three independent experiments. For **E**–**G**, data is shown as box (25th to 75th percentile) and whisker (1.5×IQR) plots with individual data points overlaid as jitter plots, the mean plotted as a white diamond and the sample sizes (n) indicated on the figures

be random with regard to old/new cell poles). It would thus be possible that the more subtle old cell pole-mediated effect we observed with regard to division site asymmetry (Figs. 1, 2, Supplementary Figs. S1 and S2) also slightly contributes to FtsZ and nucleoid shifting in PA-bearing cells.

Therefore, to provide further independent support for the above-mentioned nucleoid displacement model (and also to rule out any effects that may be caused by the fixation process necessary for immunolabelling of FtsZ in Fig. 3), we aimed to obtain detailed information about the impact of PA size on several nucleoid characteristics by equipping *E. coli* MG1655 *ibpA-msfGFP tnaA*$^{\Delta 106}$ with an mScarlet-I translational fusion to the histone-like DNA-binding protein HU-α (produced by expression of *hupA*). Using L-tryptophan-induced exponential phase cultures of the resulting MG1655 *ibpA-msfGFP tnaA*$^{\Delta 106}$ *hupA-mScarlet-I* strain (Fig. 4A), we binned cells according to whether they were PA-free or contained a small, medium or large polar PA (based on arbitrary cutoffs for the amount of polarly located IbpA-msfGFP fluorescence, representative examples are shown in Supplementary Fig. S5). The nucleoid (determined by the position of its centroid) in single-nucleoid cells was indeed found to be displaced away from the PA-bearing pole and this effect was found to be proportional with PA-size (Fig. 4B). Moreover, this size-dependent effect persisted in cells containing 2 nucleoids and was found to occur on both the nucleoid closest to (Fig. 4C, bottom) and the one farthest away from (Fig. 4C, top) the PA-bearing pole, although the shift appeared more pronounced for the PA-proximal nucleoid (Fig. 4C). Indeed, when quantifying the normalized distance between both centroids, it becomes clear that larger PAs exert a smaller repositioning effect on the farthest nucleoid than on the closest nucleoid since the distance between the nucleoid centroids decreases with PA size (Fig. 4D). In addition, this observation seems to indicate that PAs not only cause a repositioning of the nucleoid, but that they may also compress the nucleoid along the cell's length axis. Indeed, a PA-size-dependent condensation of the nucleoid along its length axis was observed by determining the ratio of the nucleoid length over the length of the cell (Fig. 4E).

Since previous studies have reported the nucleoid position of *E. coli* to be biased towards the new pole at birth [39, 40], we were interested to investigate the impact of PAs on this phenomenon by comparing nucleoid repositioning in PA-bearing cells *vs.* their PA-free sister cells at birth using time-lapse fluorescence microscopy (Fig. 5A–G). This analysis indeed confirmed these previous observations [39, 40] (i.e., that PA-free cells have slightly asymmetric nucleoid centroids at the time of division), as observed in both PA-free sister cells from PA-bearing cell couples (Fig. 5A) and in cell couples completely devoid of PAs at the time of division (Fig. 5B). However, we found this nucleoid asymmetry to be significantly more pronounced in the PA-bearing sister cells (Fig. 5A), again indicating the impact of the physical presence of PAs on the nucleoid. In addition, while the PA-bearing sisters were found to be on average larger than the PA-free cells at birth (Fig. 5C, D, again underscoring asymmetric positioning of the division site), we could also confirm that the nucleoids seem to experience compression along the length axis of the cell when PAs are present (Fig. 5E, F). When studying some of these sister cell couples with super-resolution imaging, we could also qualitatively observe that PA-bearing cell poles were clearly devoid of chromosome-associated fluorescence, again indicating that PAs seem to physically compete for space with the nucleoid (Fig. 5H).

Taken together, these results further confirm that the physical presence of PAs impacts the intracellular

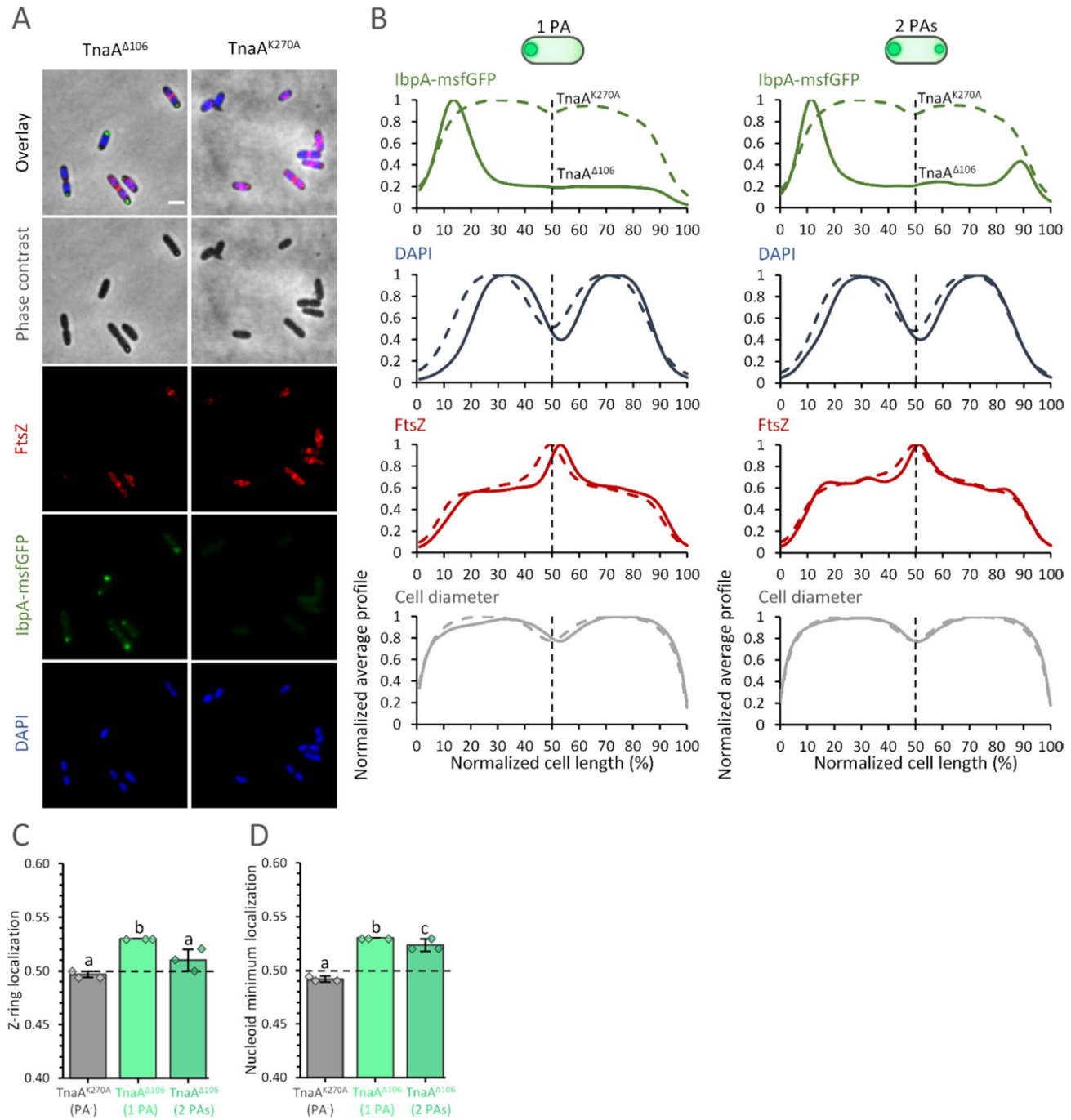

architecture of the chromosome in a size-dependent manner by condensation and repositioning of the nucleoid.

Discussion

Cell size fluctuations among clonal siblings in homogeneous environments are generally assumed to be purely stochastic in nature. However, we uncovered the existence of a deterministic asymmetry in cell division imposed by the presence of intracellular PAs, which influences cell sizes beyond the underlying stochasticity in growth and division processes. Moreover, the longer cell size of siblings asymmetrically inheriting the PA persists over multiple generations and cannot be corrected by cell size homeostasis mechanisms.

Our observations indicate that naturally occurring large intracellular structures such as PAs can play an important role in perturbing the intracellular architecture of individual cells by their physical interaction with other large structural elements such as the nucleoid. It can also further be

◂**Fig. 3** **A** Representative superimposed, phase contrast and epifluorescence (reporting FtsZ immunolabeled with Cy3, IbpA-msfGFP and DAPI stained nucleoids) images of fixed *E. coli* MG1655 *ibpA-msfGFP tnaA*$^{\Delta 106}$ (left) and *E. coli* MG1655 *ibpA-msfGFP tnaA*^{K270A} (right) cells after induction with 1.25 mM L-tryptophan. Scale bar corresponds to 2 µm. **B** Normalized average signal profiles of IbpA-msfGFP (green), DAPI stained nucleoids (blue) and Cy3 labeled FtsZ (red) and the normalized average cell diameter profile (grey) plotted against the normalized cell length for the 80–100% cell cycle age group (i.e., predivisional cells) of fixed PA-bearing *E. coli* MG1655 *ibpA-msfGFP tnaA*$^{\Delta 106}$ [solid lines; split in cells carrying 1 PA (left; $n = 1701$) and 2 PAs (right; $n = 333$)] and PA-free *E. coli* MG1655 *ibpA-msfGFP tnaA*^{K270A} (dashed lines; $n = 3540$; same data shown on the left and right as reference) cells. Cells are sorted with the cell pole containing most IbpA-msfGFP fluorescence on the left. The vertical dashed line represents the mid-point of the cell. A single representative experiment from 3 independent experiments is shown. Data for all cell cycle age groups can be found in Supplementary Figure S3. **C** Average normalized localization of the Cy3-FtsZ signal profile local maximum around midcell of the 80–100% cell cycle age group of fixed PA-free *E. coli* MG1655 *ibpA-msfGFP tnaA*^{K270A} (PA$^-$; grey) and PA-bearing *E. coli* MG1655 *ibpA-msfGFP tnaA*$^{\Delta 106}$ (1 or 2 PAs; green) cells determined over 3 independent experiments. **D** Average normalized localization of the DAPI signal profile local minimum around midcell of the 80–100% cell cycle age group of fixed PA-free *E. coli* MG1655 *ibpA-msfGFP tnaA*^{K270A} (PA$^-$; grey) and single PA-bearing *E. coli* MG1655 *ibpA-msfGFP tnaA*$^{\Delta 106}$ (1 or 2 PAs; green) cells determined over 3 independent experiments. For **C** and **D**, data on the y-axis is sorted with the cell pole containing the most IbpA-msfGFP fluorescence on the bottom. Individual data points are represented by diamonds. The horizontal dashed line represents the mid-point of the cell. Error bars represent the standard deviation. Lowercase letters indicate that pairwise comparisons between groups are statistically significant when the groups do not have any letter in common (ANOVA followed by Tukey HSD post-hoc test, p-value ≤ 0.05). In **A**–**D**, cells were transferred from well-mixed liquid cultures onto agarose pads for immediate microscopic image acquisition

hypothesized that PAs delineate a cytoplasmic "dead space" that competes for space with structures such as the nucleoid and could possibly even disrupt intracellular protein gradients [41] (e.g., pole-to-pole oscillation of the MinCDE system [9], MipZ-based division site localization [42, 43], *parABS*-based plasmid-partinioning [44, 45], etc.). From this perspective, it is tempting to consider that some bacteria may have evolved mechanisms to mitigate the disturbing presence of a large PA structure. In fact, it was recently shown that PA management of *Caulobacter crescentus* differs from that of *E. coli* and *B. subtilis*, since *C. crescentus* PAs seem to be distributed throughout the cell volume and become partitioned to both daughter cells [46].

Since protein aggregation is a ubiquitous phenomenon in all life-forms and known to be affected by a wide variety of frequently experienced environmental conditions (such as pH, temperature, oxidative stress, antibiotics, pressure, starvation, and even in the absence of obvious stressors) [30, 47], it is likely that our observations are not limited to the cellular model systems and environmental conditions tested in this study. Presumably, the observed effects of PAs on the nucleoid and division machinery could even extend to other types of intracellular structures (e.g., polyhydroxyalkanoates (PHA) [48–50], polyphosphate (polyP) granules [51–53], and glycogen deposits [54–56]), depending on their specific spatial and temporal dynamics. In fact, a smaller old pole-associated deterministic asymmetry was also reproducibly detected in PA-free cells, which, we hypothesize, stems from the presence of polar cellular structures/debris not reported on by the IbpA-msfGFP reporter. One candidate for this may be the deposit of glycogen, which is known to occur in old cell poles [54–56].

In summary, our study demonstrates that the presence of PAs can impacts cellular architecture and processes related to cell division and cell size determination. Specifically, we demonstrate that these structures influence nucleoid placement and size, the location of the division site, and cell length at birth. As such, PAs can be regarded as a deterministic driver for cell size differences among siblings of a clonal population, even within homogeneous environments.

Materials and methods

Bacterial strains and growth conditions

The bacterial strains and plasmids used in this study are listed in Table S1 and primers are listed in Table S2.

Liquid culturing of *E. coli* for physiological testing was done in AB medium (supplemented with 10 µg/ml thiamine, 25 µg/ml uracil and 0.2% casamino acids). AB medium [with the above-mentioned supplements and the addition of 2% agarose (Eurogentec, Seraing, Belgium)] was also used to make agarose pads intended for time-lapse microscopy, while 0.85% KCl agarose pads were used in the case of single time-point microscopy snapshots. Stationary phase *B. subtilis* cultures were prepared in BHI medium (Oxoid, Hampshire, United Kingdom), while MOPS medium (adapted from Kort et al. [57]) was used for exponential phase cultures and agarose pads and contains 1.32 mM K_2HPO_4, 0.4 mM $MgCl_2$, 0.276 mM K_2SO_4, 0.01 mM $FeSO_4$, 0.14 mM $CaCl_2$, 80 mM 3-[*N*-morpholino]propanesulfonic acid (MOPS), 4 mM Tricine, 10 mM NH_4Cl, 3 nM $(NH_4)_6Mo_7O_{24}$, 0.4 µM H_3BO_3, 30 nM $CoCl_2$, 10 nM $CuSO_4$, 10 nM $ZnSO_4$, 0.1 mM $MnCl_2$, 27.8 mM glucose, 0.02% casamino acids and 30 mM L-valine. Lysogeny Broth according to Lennox (LB) was used for strain and plasmid construction unless indicated otherwise.

Cultures were always incubated at 37 °C, except for the appropriate times during strain construction when growth at 30 °C was required. Liquid cultures were incubated aerobically while shaking (250 rpm) in tubes containing 4 ml of medium (except for when preparing cultures for immunolabeling, in which case 25 ml cultures were used). Stationary

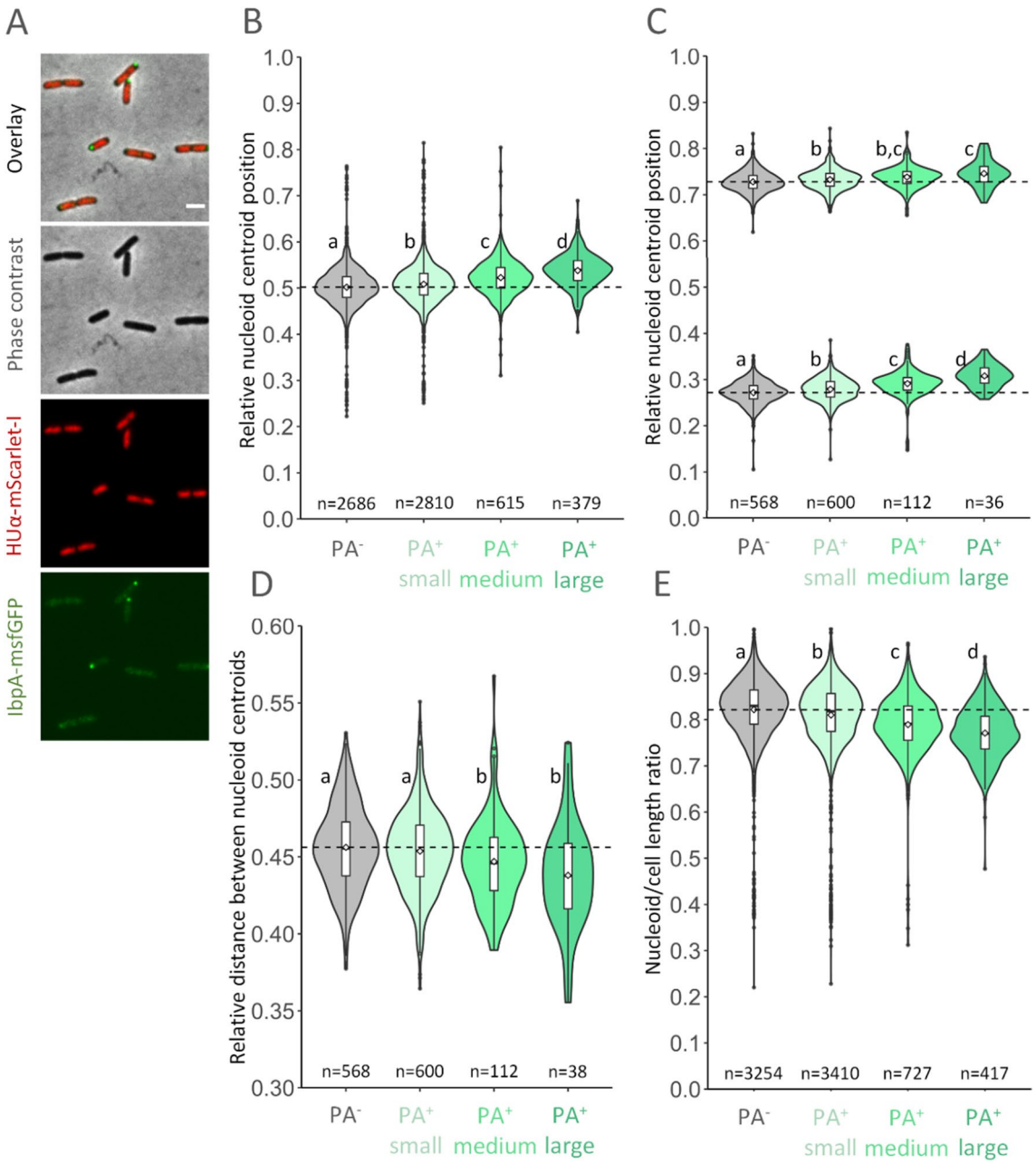

phase cultures were obtained by allowing ca. 16 h of growth, while exponential phase cultures were obtained by diluting stationary phase cultures 1/100 (*B. subtilis*) or 1/1000 (*E. coli*) in fresh medium and allowing growth for ca. 3 (*B. subtilis*) or 5 h (*E. coli*).

When appropriate, the following chemicals were added to the medium at the indicated final concentrations: 100 µg/ml ampicillin (Fisher Scientific, Pittsburgh, PA, USA; *E. coli*), 50 µg/ml kanamycin (Applichem, Darmstadt, Germany; *E. coli*), 5 µg/ml kanamycin (*B. subtilis*), 50 µg/ml spectinomycin (Sigma-Aldrich; *B. subtilis*), 1.25 mM L-tryptophan (Acros Organics, Geel, Belgium), 0.2% glucose, 100 µM Isopropyl β-D-1-thiogalactopyranoside (IPTG; Acros Organics) and 1 µg/ml DAPI (4′,6-diamidino-2-phenylindole).

Strain and plasmid construction

A C-terminal translational fusion of *mScarlet-I* to *hupA* was made by creating an m*Scarlet-I-frt-nptI-frt* amplicon from the previously described pBam1-Tn5-*mScarlet-I* plasmid with primers P1 and P2. Subsequently, recombineering into the *hupA* locus was achieved by lambda Red-mediated recombination using pKD46 [58]. The frt-flanked kanamycin resistance cassette was subsequently

◂**Fig. 4** **A** Representative superimposed, phase contrast and epifluorescence (reporting HUα-mScarlet-I (red) and IbpA-msfGFP (green) localization) images of live *E. coli* MG1655 *ibpA-msfGFP tnaA*$^{\Delta 106}$ *hupA-mScarlet-I* cells after induction with 1.25 mM L-tryptophan. Scale bar corresponds to 2 µm. **B** Relative centroid position of the nucleoid for normalized *E. coli* MG1655 *ibpA-msfGFP tnaA*$^{\Delta 106}$ cells with 1 nucleoid after L-tryptophan induction and binned according to whether they had no (PA^-), small (PA^+ small), medium (PA^+ medium) or large PAs (PA^+ large). **C** Relative centroid position of both nucleoids for normalized *E. coli* MG1655 *ibpA-msfGFP tnaA*$^{\Delta 106}$ cells with 2 nucleoids after L-tryptophan induction and binned according to whether they had no (PA^-), small (PA^+ small), medium (PA^+ medium) or large PAs (PA^+ large). **D** Relative distance between both nucleoid centroid positions for normalized *E. coli* MG1655 *ibpA-msfGFP tnaA*$^{\Delta 106}$ cells with 2 nucleoids after L-tryptophan induction and binned according to whether they had no (PA^-), small (PA^+ small), medium (PA^+ medium) or large PAs (PA^+ large). **E** Ratio of nucleoid length over cell length for all *E. coli* MG1655 *ibpA-msfGFP tnaA*$^{\Delta 106}$ cells after L-tryptophan induction and binned according to whether they had no (PA^-), small (PA^+ small), medium (PA^+ medium) or large PAs (PA^+ large). For **B** and **C**, positions are determined in reference to the cell pole of the cell half with the most IbpA-msfGFP fluorescence. For **B**–**E**, the horizontal dashed line corresponds to the average value observed for the PA-free subpopulation and serves as a visual reference. Data were pooled from three independently grown cultures and is shown as violin plots overlaid with box (25th to 75th percentile) and whisker (1.5 × IQR) plots, the mean is plotted as a white diamond and the sample sizes (*n*) are indicated on the figures. Lowercase letters on **B**–**E** indicate that pairwise comparisons between groups are statistically significant when the groups do not have any letter in common (linear mixed model correct for cell length with different cultures included as random factors followed by Tukey HSD post-hoc test, p-value ≤ 0.05). In **A**–**E**, cells were transferred from well-mixed liquid cultures onto agarose pads for immediate microscopic image acquisition

excised through site-specific recombination by transiently equipping the strain with plasmid pCP20 [66].

All constructed plasmids and chromosomal insertions were initially confirmed by PCR with primer pairs attaching outside of the region of insertion (Table S2). Correct insertions were further verified by sequencing (Macrogen, Amsterdam, the Netherlands).

PA induction

PAs (or the corresponding soluble controls) were induced by the addition of 1.25 mM L-tryptophan (strains containing *tnaA*$^{\Delta 106}$ or *tnaA*^{K270A} alleles) for the last 2 h of growth, by the addition of 100 µM IPTG for the last hour of growth (strains containing fluorescently labeled *cI78*^{EP8} or *cI78*^{WT} alleles) or through sublethal heat-treatment (47 °C, 15 min), as indicated. Heat treatment of liquid cultures was performed as previously described in Mortier and Gayán et al. [37]. Cells induced with L-tryptophan or IPTG were subsequently washed three times (8000 × *g*, 1 min) with AB medium to remove the inducer.

Immunolabeling

Cells were immunolabeled as previously described [59]. Briefly, cell cultures were fixed with formaldehyde and glutaraldehyde shaking in a water bath at 37 °C for 15 min. The cells were subsequently washed in PBS, permeabilized by Triton-X100 and lysozyme and incubated in blocking buffer to prevent non-specific binding of the antibodies before incubation with primary antibodies against FtsZ for 1 h at 37 °C. Next, the cells were washed and incubated with secondary anti-rabbit antibodies conjugated to Cy3 (Jacksons's immunochemicals, Baltimore, MD, USA).

Microscopy

Bacterial cultures were immobilized on agarose pads containing the appropriate medium and covered with a cover glass attached to a 125 µl Gene Frame (Thermo Fisher Scientific).

For Figs. 1, 2, 4, 5A–G, S1 and S2, image acquisition was performed using a Ti-Eclipse inverted microscope with NIS-elements software (Nikon, Champigny-sur-Marne, France) equipped with a 100 × Plan Apo λ oil objective, a TI-CT-E motorized condenser and a Nikon DS-Qi2 camera. msfGFP was imaged using a quad-edge dichroic (395/470/550/640 nm) and a FITC single emission filter, while mScarlet-I and mCerulean were imaged using a triple-edge dichroic (475/540/600 nm). A SpectraX LED illuminator (Lumencor, Beaverton, OR, USA) was used as light source, using the 470/24 excitation filter. Temperature was controlled with an Okolab cage incubator (Okolab, Ottaviano, Italy).

Image acquisition for Figs. 3, S3 and S4 was achieved using an Olympus BX-60 fluorescence microscope (Olympus, Tokyo, Japan) equipped with an UPlanApo 100 × /N.A. 1.35 oil Iris Ph3 objective, Hamamatsu ORCA-flash4.0JT model C11440-42U camera (Hamamatsu, Hamamatsu City, Japan). Images were acquired using the Micro Manager 1.4 plugin for ImageJ. DAPI was imaged through a U-MWU filter (excitation 330–385 nm, dichroic 400 nm and emission > 400 nm; Olympus), msfGFP and GFP(Sp) through a GFP filter (excitation 470 ± 40 nm, dichroic 495 nm and emission 525 ± 50 nm; Chroma, Taoyuan City, Taiwan), and Cy3 were imaged through an mCherry filter (excitation 560 ± 40 nm, dichroic 505 nm and emission 630 ± 75 nm; Chroma).

Image acquisition for Fig. 5H was done with a Zeiss LSM 880 confocal laser scanning microscope equipped with an α Plan-Apochromat 100x/1.46 Oil DIC M27, a TPMT for imaging the cell and Airyscan for super-resolution fluorescence imaging (Zeiss, Oberkochen, Germany).

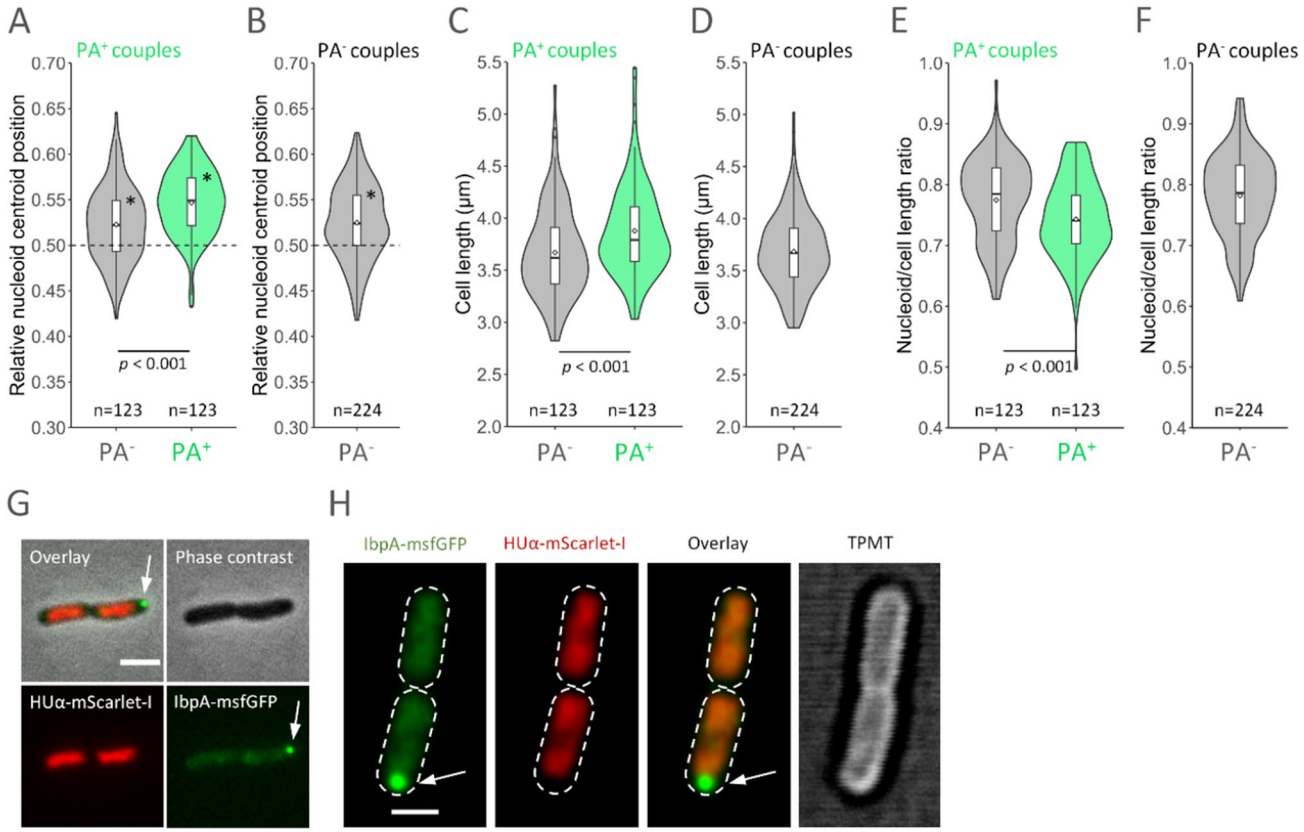

Fig. 5 **A** Normalized nucleoid centroid position (relative to either the PA-free or PA-bearing old cell pole) of PA-free (PA^-; grey) and PA-bearing (PA^+; green) *E. coli* MG1655 *ibpA-msfGFP tnaA*$^{\Delta 106}$ *hupA-mScarlet-I* sister cells from PA-bearing cell couples at birth. **B** Normalized nucleoid centroid position (relative to the old cell pole) of PA-free *E. coli* MG1655 *ibpA-msfGFP tnaA*$^{\Delta 106}$ *hupA-mScarlet-I* sister cells from PA-free cell couples at birth. **C** Cell length of PA-free (PA^-; grey) and PA-bearing (PA^+; green) *E. coli* MG1655 *ibpA-msfGFP tnaA*$^{\Delta 106}$ *hupA-mScarlet-I* sister cells from PA-bearing cell couples at birth. **D** Cell length of PA-free *E. coli* MG1655 *ibpA-msfGFP tnaA*$^{\Delta 106}$ *hupA-mScarlet-I* sister cells from PA-free cell couples at birth. **E** Ratio of nucleoid length over cell length of PA-free (PA^-; grey) and PA-bearing (PA^+; green) *E. coli* MG1655 *ibpA-msfGFP tnaA*$^{\Delta 106}$ *hupA-mScarlet-I* sister cells from PA-bearing cell couples at birth. **F** Ratio of nucleoid length over cell length of PA-free *E. coli* MG1655 *ibpA-msfGFP tnaA*$^{\Delta 106}$ *hupA-mScarlet-I* sister cells from PA-free cell couples at birth. **G** Representative phase contrast, epifluorescence [reporting HUα-mScarlet-I (red) and IbpA-msfGFP localization (green)] and superimposed images of *E. coli* MG1655 *ibpA-msfGFP tnaA*$^{\Delta 106}$ *hupA-mScarlet-I* sister cells after induction with 1.25 mM L-tryptophan is halted. The asymmetrically segregated TnaA$^{\Delta 106}$ PA in the PA-bearing cell is indicated by a white arrow. Scale bar corresponds to 2 µm. **H** Representative super-resolution fluorescence [reporting IbpA-msfGFP (green) and HUα-mScarlet-I (red)], superimposed and TPMT images of *E. coli* MG1655 *ibpA-msfGFP tnaA*$^{\Delta 106}$ *hupA-mScarlet-I* sister cells after induction with 1.25 mM L-tryptophan is halted. Cell outline is represented in white and a white arrow indicates the TnaA$^{\Delta 106}$ PA. Scale bar corresponds to 1 µm. For **A** and **B**, asterisks indicate significant differences ($p \leq 0.05$) from 0.5 (one-sample *t*-tests) and the horizontal dashed line at 0.5 represent a perfectly symmetric nucleoid centroid position, while values higher than 0.5 correspond to a nucleoid centroid position shifted away from the old cell pole. For **A**, **C** and **E**, PA-bearing and PA-free groups were compared using paired two-sided *t*-tests. For **A**–**F**, data were pooled from three independent experiments and is shown as violin plots overlaid with box (25th to 75th percentile) and whisker (1.5 × IQR) plots and the mean is plotted as a white diamond

Image analysis

Cell lengths for Fig. 1A were determined using the open-source software Ilastik [60], which was trained to robustly identify and segment bacterial cells and exclude debris and out-of-focus cells, and the microbeJ [61] plugin (version 5.13l; https://www.microbej.com/) for ImageJ (version 1.53c; https://imagej.nih.gov/ij/).

Cell lengths at birth for Figs. 1B, 2, S1 and S2 were manually measured in NIS-Elements AR 5.20.00 (Nikon). The average of two independent measurements was taken to minimize technical variability. For MG1655 *ibpA-msfGFP tnaA*$^{\Delta 106}$, MG1655 Δ*lacY* pTrc99A-P_{trc}-*mCer-cI78*^{EP8} *and* PS832 *amyE::*$P_{Hyperspank}$ *gfp(Sp)-cI78*^{EP8}, only microcolonies with founder cells carrying a single polarly localized labeled PA that lasted for at least 3 generations were selected for analysis. Since heat-shocked founder cells in Fig. 1B mostly carried multiple PAs, cells were allowed 1 division prior to analysis to generate founder cells with a single PA.

Signal profiles for Figs. 3, S3 and S4 were obtained using Coli Inspector (https://sils.fnwi.uva.nl/bcb/objectj/examples/Coli-Inspector/Coli-Inspector-MD/coli-inspector.html) supported by the ObjectJ plugin [62] (https://sils.fnwi.uva.nl/bcb/objectj/) for ImageJ. Cell cycle age groups were binned according to cell length. Background fluorescence was removed from the images using the ObjectJ plugin.

For Fig. 4, cell meshes of individual cells were automatically generated by the open-source image analysis software Oufti [63] for the subsequent use in custom MATLAB (https://www.mathworks.com/) scripts to extract cell lengths and nucleoid characteristics like previously reported [64]. Manual curation of the dataset was necessary to achieve a robust detection of cellular and nucleoid characteristics. Cells were binned in groups with different PA-sizes by setting arbitrary cut-off points for the average pixel intensity of IbpA-msfGFP fluorescence in the most fluorescent cell pole (i.e., one third of the cell) based on visual inspection of the images (Supplementary Fig. S5). Cells were oriented according to the cell half that has the largest total IbpA-msfGFP intensity. For PA-bearing cells, this corresponds to the cell half where the PA is located. Note that the analysis does not take into account that a fraction of cells contains 2 PAs, but since this fraction is very small (< 1%), this should have no meaningful effect on the results.

Similarly, for Fig. 5A–G, cell meshes of sister cell couples at the time of division were manually generated in Oufti and the old cell poles of all cells were marked using Oufti's polarity feature. This was followed by the extraction of several cell morphology characteristics (including cell length, nucleoid length and the position of the nucleoid centroid relative to the old cell pole) using custom MATLAB scripts as previously reported [64]. Manual curation of the dataset was performed to remove cells with aberrant cell segmentation and/or unsuccessful nucleoid detection.

Statistical analysis

Statistical analyses (ANOVA, linear mixed models, Tukey HSD post hoc test, Student's t test, Welch's t test, Bonferroni corrections, ANCOVA and the appropriate tests to test for underlying assumptions) were carried out using the R open-source software [65]. Differences were regarded as significant when the p value was ≤ 0.05.

Student's t tests for Figs. 3 and S4 were performed on the normalized position of the local normalized fluorescence profile maximum (Cy3-labeled FtsZ) or minimum (DAPI) at midcell on the last age group over 3 independent experiments.

Supplementary Information The online version contains supplementary material available at https://doi.org/10.1007/s00018-023-05002-4.

Acknowledgements We would like to thank the Research Foundation-Flanders (FWO-Vlaanderen) and the KU Leuven Research Fund for providing funding for this study.

Funding This work was supported by doctoral fellowships (11B0519N to J.M., 11J6222N to R.V.E., and 1135116N to A.C.) and research grants (G0C7118N and G0D8220N) from the Research Foundation-Flanders (FWO-Vlaanderen), and a postdoctoral fellowship (PDM/20/118 to J.M.) and a start-up grant (STG/21/068 to S.K.G.) from the KU Leuven Research Fund.

Data availability The datasets generated by this study will be made available by the corresponding author upon request.

Declarations

Conflict of interests The authors have no relevant financial or non-financial interests to disclose.

Ethics approval Not applicable.

Consent to participate Not applicable.

Consent to publish Not applicable.

References

1. Young KD (2006) The selective value of bacterial shape. Microbiol Mol Biol Rev 70:660–703. https://doi.org/10.1128/mmbr.00001-06
2. Facchetti G, Chang F, Howard M (2017) Controlling cell size through sizer mechanisms. Curr Opin Syst Biol 5:86–92. https://doi.org/10.1016/j.coisb.2017.08.010
3. Sauls JT, Li D, Jun S (2016) Adder and a coarse-grained approach to cell size homeostasis in bacteria. Curr Opin Cell Biol 38:38–44. https://doi.org/10.1016/j.ceb.2016.02.004
4. Jun S, Taheri-Araghi S (2015) Cell-size maintenance: universal strategy revealed. Trends Microbiol 23:4–6. https://doi.org/10.1016/j.tim.2014.12.001
5. Campos M et al (2014) A constant size extension drives bacterial cell size homeostasis. Cell 159:1433–1446. https://doi.org/10.1016/j.cell.2014.11.022
6. Taheri-Araghi S et al (2015) Cell-size control and homeostasis in bacteria. Curr Biol 25:385–391. https://doi.org/10.1016/j.cub.2014.12.009
7. Willis L, Huang KC (2017) Sizing up the bacterial cell cycle. Nat Rev Microbiol 15:606–620. https://doi.org/10.1038/nrmicro.2017.79
8. Mahone CR, Goley ED (2020) Bacterial cell division at a glance. J Cell Sci 133:1–7. https://doi.org/10.1242/jcs.237057
9. Rowlett VW, Margolin W (2013) The bacterial min system. Curr Biol 23:R553–R556. https://doi.org/10.1016/j.cub.2013.05.024
10. Cho H, Bernhardt TG (2013) Identification of the SlmA active site responsible for blocking bacterial cytokinetic ring assembly over the chromosome. PLoS Genet. https://doi.org/10.1371/journal.pgen.1003304
11. Cho H, McManus HR, Dove SL, Bernhardt TG (2011) Nucleoid occlusion factor SlmA is a DNA-activated FtsZ polymerization antagonist. Proc Natl Acad Sci U S A 108:3773–3778. https://doi.org/10.1073/pnas.1018674108
12. Tonthat NK et al (2011) Molecular mechanism by which the nucleoid occlusion factor, SlmA, keeps cytokinesis in check. EMBO J 30:154–164. https://doi.org/10.1038/emboj.2010.288

13. Tonthat NK et al (2013) SlmA forms a higher-order structure on DNA that inhibits cytokinetic Z-ring formation over the nucleoid. Proc Natl Acad Sci USA 110:10586–10591. https://doi.org/10.1073/pnas.1221036110
14. Dupaigne P et al (2012) Molecular basis for a protein-mediated DNA-bridging mechanism that functions in condensation of the *E. coli* chromosome. Mol Cell 48:560–571. https://doi.org/10.1016/j.molcel.2012.09.009
15. Mercier R et al (2008) The MatP/matS site-specific system organizes the terminus region of the *E. coli* chromosome into a macrodomain. Cell 135:475–485. https://doi.org/10.1016/j.cell.2008.08.031
16. Espéli O et al (2012) A MatP–divisome interaction coordinates chromosome segregation with cell division in E. coli. EMBO J 31:3198–3211. https://doi.org/10.1038/emboj.2012.128
17. Monterroso B et al (2019) The bacterial DNA binding protein matp involved in linking the nucleoid terminal domain to the divisome at midcell interacts with lipid membranes. MBio. https://doi.org/10.1128/mBio.00376-19
18. Castillo DE, Yang D, Siopsis G, Männik J (2016) The role of MatP, ZapA and ZapB in chromosomal organization and dynamics in *Escherichia coli*. Nucleic Acids Res 44:1216–1226. https://doi.org/10.1093/nar/gkv1484
19. Monds RD et al (2014) Systematic perturbation of cytoskeletal function reveals a linear scaling relationship between cell geometry and fitness. Cell Rep 9:1528–1537. https://doi.org/10.1016/j.celrep.2014.10.040
20. Amodeo AA, Skotheim JM (2016) Cell-size control. Cold Spring Harb Perspect Biol. https://doi.org/10.1101/cshperspect.a019083
21. Cesar S, Huang KC (2017) Thinking big: the tunability of bacterial cell size. FEMS Microbiol Rev 41:672–678. https://doi.org/10.1093/femsre/fux026
22. Bi E, Lutkenhaus J (1991) FtsZ ring structure associated with division in *Escherichia coli*. Nature 354:161–164. https://doi.org/10.1038/354161a0
23. Schaechter M, Maaløe O, Kjeldgaard NO (1958) Dependency on medium and temperature of cell size and chemical composition during balanced growth of *Salmonella typhimurium*. J Gen Microbiol 19:592–606. https://doi.org/10.1099/00221287-19-3-592
24. Vadia S, Levin PA (2015) Growth rate and cell size: a re-examination of the growth law. Curr Opin Microbiol 24:96–103. https://doi.org/10.1016/j.mib.2015.01.011
25. Heinrich K, Leslie DJ, Morlock M, Bertilsson S, Jonas K (2019) Molecular basis and ecological relevance of Caulobacter cell filamentation in freshwater habitats. MBio 10:1–17. https://doi.org/10.1128/mbio.01557-19
26. Navarro Llorens JM, Tormo A, Martínez-García E (2010) Stationary phase in gram-negative bacteria. FEMS Microbiol Rev 34:476–495. https://doi.org/10.1111/j.1574-6976.2010.00213.x
27. Bergmiller T, Pẽa-Miller R, Boehm A, Ackermann M (2011) Single-cell time-lapse analysis of depletion of the universally conserved essential protein YgjD. BMC Microbiol 11:1–12. https://doi.org/10.1186/1471-2180-11-118
28. Rojas E, Theriot JA, Huang KC (2014) Response of *Escherichia coli* growth rate to osmotic shock. Proc Natl Acad Sci USA 111:7807–7812. https://doi.org/10.1073/pnas.1402591111
29. Si F et al (2019) Mechanistic origin of cell-size control and homeostasis in bacteria. Curr Biol 29:1760-1770.e7. https://doi.org/10.1016/j.cub.2019.04.062
30. Schramm FD, Schroeder K, Jonas K (2019) Protein aggregation in bacteria. FEMS Microbiol Rev 44:54–72. https://doi.org/10.1093/femsre/fuz026
31. Govers SK, Dutré P, Aertsen A (2014) In vivo disassembly and reassembly of protein aggregates in *Escherichia coli*. J Bacteriol 196:2325–2332. https://doi.org/10.1128/jb.01549-14
32. Winkler J et al (2010) Quantitative and spatio-temporal features of protein aggregation in *Escherichia coli* and consequences on protein quality control and cellular ageing. EMBO J 29:910–923. https://doi.org/10.1038/emboj.2009.412
33. Coquel AS et al (2013) localization of protein aggregation in *Escherichia coli* is governed by diffusion and nucleoid macromolecular crowding effect. PLoS Comput Biol 9:1–14. https://doi.org/10.1371/journal.pcbi.1003038
34. Lindner AB, Madden R, Demarez A, Stewart EJ, Taddei F (2008) Asymmetric segregation of protein aggregates is associated with cellular aging and rejuvenation. Proc Natl Acad Sci USA 105:3076–3081. https://doi.org/10.1073/pnas.0708931105
35. Mortier J, Tadesse W, Govers SK, Aertsen A (2019) Stress-induced protein aggregates shape population heterogeneity in bacteria. Curr Genet 65:865-869. https://doi.org/10.1007/s00294-019-00947-1
36. Govers SK, Mortier J, Adam A, Aertsen A (2018) Protein aggregates encode epigenetic memory of stressful encounters in individual *Escherichia coli* cells. PLoS Biol. 1:e2003853. https://doi.org/10.1371/journal.pbio.2003853
37. Mortier J et al (2021) Gene erosion can lead to gain-of-function alleles that contribute to bacterial fitness. mBio 12:e0112921. https://doi.org/10.1128/mbio.01129-21
38. Li G, Young KD (2015) A new suite of tnaA mutants suggests that *Escherichia coli* tryptophanase is regulated by intracellular sequestration and by occlusion of its active site. BMC Microbiol 15:1–17. https://doi.org/10.1186/s12866-015-0346-3
39. Hadizadeh Yazdi N, Guet CC, Johnson RC, Marko JF (2012) Variation of the folding and dynamics of the *Escherichia coli* chromosome with growth conditions. Mol Microbiol 86:1318–1333. https://doi.org/10.1111/mmi.12071
40. Cass JA, Kuwada NJ, Traxler B, Wiggins PA (2016) *Escherichia coli* chromosomal loci segregate from midcell with universal dynamics. Biophys J 110:2597–2609. https://doi.org/10.1016/j.bpj.2016.04.046
41. Kiekebusch D, Thanbichler M (2014) Spatiotemporal organization of microbial cells by protein concentration gradients. Trends Microbiol 22:65–73. https://doi.org/10.1016/j.tim.2013.11.005
42. Kiekebusch D, Michie KA, Essen LO, Löwe J, Thanbichler M (2012) Localized dimerization and nucleoid binding drive gradient formation by the bacterial cell division inhibitor MipZ. Mol Cell 46:245–259. https://doi.org/10.1016/j.molcel.2012.03.004
43. Thanbichler M, Shapiro L (2006) MipZ, a spatial regulator coordinating chromosome segregation with cell division in Caulobacter. Cell 126:147–162. https://doi.org/10.1016/j.cell.2006.05.038
44. Hwang LC et al (2013) ParA-mediated plasmid partition driven by protein pattern self-organization. EMBO J 32:1238–1249. https://doi.org/10.1038/emboj.2013.34
45. Vecchiarelli AG et al (2010) ATP control of dynamic P1 ParA–DNA interactions: a key role for the nucleoid in plasmid partition. Mol Microbiol 78:78–91. https://doi.org/10.1111/j.1365-2958.2010.07314.x
46. Schramm FD, Schroeder K, Alvelid J, Testa I, Jonas K (2019) Growth-driven displacement of protein aggregates along the cell length ensures partitioning to both daughter cells in *Caulobacter crescentus*. Mol Microbiol 111:1430–1448. https://doi.org/10.1111/mmi.14228
47. Maisonneuve E, Fraysse L, Moinier D, Dukan S (2008) Existence of abnormal protein aggregates in healthy *Escherichia coli* cells. J Bacteriol 190:887–893. https://doi.org/10.1128/jb.01603-07
48. Pfeiffer D, Jendrossek D (2012) Localization of poly(3-Hydroxybutyrate) (PHB) granule-associated proteins during PHB granule formation and identification of two new phasins, phap6 and phap7, in *Ralstonia eutropha* H16. J Bacteriol 194:5909–5921. https://doi.org/10.1128/jb.00779-12

49. Jendrossek D, Pfeiffer D (2014) New insights in the formation of polyhydroxyalkanoate granules (carbonosomes) and novel functions of poly(3-hydroxybutyrate). Environ Microbiol 16:2357–2373. https://doi.org/10.1111/1462-2920.12356
50. Peters V, Becher D, Rehm BHA (2007) The inherent property of polyhydroxyalkanoate synthase to form spherical PHA granules at the cell poles: the core region is required for polar localization. J Biotechnol 132:238–245. https://doi.org/10.1016/j.jbiotec.2007.03.001
51. Frank C, Pfeiffer D, Aktas M, Jendrossek D (2022) Migration of polyphosphate granules in *Agrobacterium tumefaciens*. Microb Physiol. https://doi.org/10.1159/000521970
52. Pallerla SR et al (2005) Formation of volutin granules in *Corynebacterium glutamicum*. FEMS Microbiol Lett 243:133–140. https://doi.org/10.1016/j.femsle.2004.11.047
53. Seufferheld M et al (2003) Identification of organelles in bacteria similar to acidocalcisomes of unicellular eukaryotes. J Biol Chem 278:29971–29978. https://doi.org/10.1074/jbc.M304548200
54. Boehm A et al (2016) Genetic manipulation of glycogen allocation affects replicative lifespan in *E. coli*. PLoS Genet 12:1–17. https://doi.org/10.1371/journal.pgen.1005974
55. Alonso-Casajús N et al (2006) Glycogen phosphorylase, the product of the glgP gene, catalyzes glycogen breakdown by removing glucose units from the nonreducing ends in *Escherichia coli*. J Bacteriol 188:5266–5272. https://doi.org/10.1128/jb.01566-05
56. Bonafonte MA et al (2000) The relationship between glycogen synthesis, biofilm formation and virulence in *Salmonella enteritidis*. FEMS Microbiol Lett 191:31–36. https://doi.org/10.1111/j.1574-6968.2000.tb09315.x
57. Kort R et al (2005) Assessment of heat resistance of bacterial spores from food product isolates by fluorescence monitoring of dipicolinic acid release. Appl Environ Microbiol 71:3556–3564. https://doi.org/10.1128/AEM.71.7.3556-3564.2005
58. Datsenko KA, Wanner BL (2000) One-step inactivation of chromosomal genes in *Escherichia coli* K-12 using PCR products. Proc Natl Acad Sci 97:6640–6645. https://doi.org/10.1073/pnas.120163297
59. Buddelmeijer N, Aarsman M, den Blaauwen, T (2013) Immunolabeling of proteins in situ in *Escherichia coli* K12 strains. BioProtocol. https://doi.org/10.21769/BioProtoc.852
60. Sommer C et al (2011) Ilastik: interactive learning and segmentation toolkit. In: Eighth IEEE International Symposium on Biomedical Imaging (ISBI). Proceedings, pp 230–233. https://doi.org/10.1109/ISBI.2011.5872394
61. Ducret A, Quardokus EM, Brun YV (2016) MicrobeJ, a tool for high throughput bacterial cell detection and quantitative analysis. Nat Microbiol 1:16077. https://doi.org/10.1038/nmicrobiol.2016.77
62. Vischer NOE et al (2015) Cell age dependent concentration of *Escherichia coli* divisome proteins analyzed with ImageJ and ObjectJ. Front Microbiol 6:1–18. https://doi.org/10.3389/fmicb.2015.00586
63. Paintdakhi A et al (2016) Oufti: an integrated software package for high-accuracy, high-throughput quantitative microscopy analysis. Mol Microbiol 99:767–777. https://doi.org/10.1111/mmi.13264
64. Gray WT et al (2019) Nucleoid size scaling and intracellular organization of translation across bacteria. Cell 177:1632-1648.e20. https://doi.org/10.1016/j.cell.2019.05.017
65. R Core Team (2023) R: a language and environment for statistical computing. R: A language and environment for statistical computing. (R Foundation for Statistical Computing, Vienna, Austria)
66. Cherepanov PP, Wackernagel W (1995) Gene disruption in *Escherichia coli*: Tc R and Km R cassettes with the option of Flp-catalyzed excision of the antibiotic-resistance determinant. Gene 158:9–14. https://doi.org/10.1016/0378-1119(95)00193-A

Publisher's Note Springer Nature remains neutral with regard to jurisdictional claims in published maps and institutional affiliations.

Springer Nature or its licensor (e.g. a society or other partner) holds exclusive rights to this article under a publishing agreement with the author(s) or other rightsholder(s); author self-archiving of the accepted manuscript version of this article is solely governed by the terms of such publishing agreement and applicable law.